Michael K. Stoellinger, Stefan Heinz*, Celestin P. Zemtsop, Harish Gopalan and Reza Mokhtarpoor

Stochastic-Based RANS-LES Simulations of Swirling Turbulent Jet Flows

Abstract: Many turbulent flow simulations require the use of hybrid methods because LES methods are computationally too expensive and RANS methods are not sufficiently accurate. We consider a recently suggested hybrid RANS-LES model that has a sound theoretical basis: it is systematically derived from a realizable stochastic turbulence model. The model is applied to turbulent swirling and nonswirling jet flow simulations. The results are shown to be in a very good agreement with available experimental data of nonswirling and mildly swirling jet flows. Compared to commonly applied other hybrid RANS-LES methods, our RANS-LES model does not seem to suffer from the 'modeled-stress depletion' problem that is observed in DES and IDDES simulations of nonswirling jet flows, and it performs better than segregated RANS-LES models. The results presented contribute to a better physical understanding of swirling jet flows through an explanation of conditions for the onset and the mechanism of vortex breakdown.

Keywords: swirling turbulent jets, hybrid RANS-LES method, vortex breakdown

***Corresponding author: Stefan Heinz,** Department of Mathematics, University of Wyoming, 1000 E. University Avenue, Laramie, WY 82071, USA, E-mail: heinz@uwyo.edu

Michael K. Stoellinger, Department of Mechanical Engineering, University of Wyoming, 1000 E. University Avenue, Laramie, WY 82071, USA, E-mail: mstoell@uwyo.edu

Celestin P. Zemtsop, Department of Mathematics, University of Wyoming, 1000 E. University Avenue, Laramie, WY 82071, USA, E-mail: celestin.zemtsop@metrohm.com

Harish Gopalan, Department of Mechanical Engineering, University of Wyoming, 1000 E. University Avenue, Laramie, WY 82071, USA, E-mail: gopalanh@ihpc.a-star.edu.sg

Reza Mokhtarpoor, Department of Mathematics, University of Wyoming, 1000 E. University Avenue, Laramie, WY 82071, USA, E-mail: reza.mokhtarpoor@gmail.com

1 Introduction

The understanding and prediction of vortex breakdown in swirling turbulent flows is relevant to many environmental and technical flows: vortex breakdown is seen in tornadoes, in flows over delta wings at high angles of attack (leading to an abrupt deterioration of the lift and drag characteristics and a poor controllability), and in combustion chambers, where it is used to stabilize flames. Despite a lot of progress made over the last four decades [1–6], no generally accepted explanation for the onset, internal structure, and mode selection of vortex breakdown has been presented so far [7–13]. Such insufficient understanding of vortex breakdown results in a poor effectiveness of techniques applied to control vortex breakdown [14].

The most promising approach to analyze swirling turbulent flows (with or without vortex breakdown) is to perform numerical simulations: measurements cannot provide a comparably comprehensive insight into the mechanism of such flows. Nevertheless, such simulations are very challenging. For example, the inflow conditions of swirling turbulent jets are usually determined by a nozzle flow, which has a significant influence on the development of the turbulent jet [15–17]. Accurate simulations of such turbulent jets require the simulation of the nozzle flow to provide the jet inflow conditions. Both direct numerical simulation (DNS) and large-eddy simulation (LES) methods were previously applied to the simulation of turbulent swirling jets. However, the high computational cost of these methods implied significant restrictions: DNS methods were only used for low Reynolds number simulations ($Re \leq 2000$) [7, 10, 11, 18], and both DNS and LES [19–23] methods were not used to simulate the nozzle flow of canonical swirling jets as considered here (see the illustration in Figure 1). Only for specific swirl burner simulations, LES were performed which simulated both the jet flow and a part of the nozzle flow. An example is given by the swirl burner LES of García-Villalba et al. [24–26], where a crude representation of the inlet duct (smaller than the length of the computational domain used for the jet flow simulation) was chosen for the simulations. On the
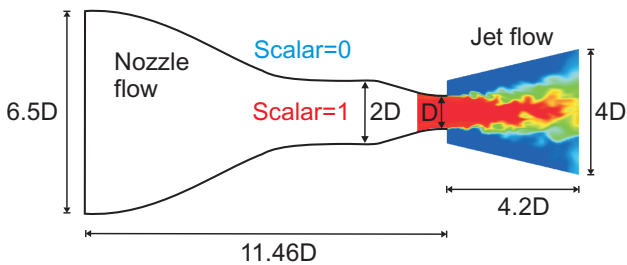
Figure 1: The computational domain. The jet flow region is illustrated in terms of the instantaneous scalar field for the S = 0.23 swirl case: see Figure 20.

other hand, Reynolds-averaged Navier-Stokes (RANS) simulations of both nozzle and jet flow regions suffer from significant problems. Two-equation turbulence models have a fundamental drawback because they are based on a single length scale definition such that they are unable to correctly account for different mixing length scales that characterize the turbulent mixing of axial and azimuthal velocities [27, 28]. More advanced models could potentially address this issue, but consistent results for a variety of flows obtained with a unified set of turbulence model constants have not been reported so far [28–30].

Thus, the most promising approach is a combination of LES and RANS methods. Such a segregated RANS-LES method, which uses nozzle flow RANS simulations to provide the inflow for the jet flow LES, was recently used by the authors to simulate swirling turbulent jet flows (resembling a solid-body rotation) below the vortex breakdown regime [17]. Comparisons with experimental data for the nonswirling case and a flow with mild swirl (with a swirl number S = 0.23; S is defined by eq. (14)) demonstrated the accuracy of this segregated RANS-LES model. However, these simulations were performed by using RANS mean velocity fields as input for jet flow LES, and by providing instantaneous jet inflow data such that the characteristic length and time scales of inflowing turbulent eddies are consistent with the RANS profiles imposed at the inlet [17, 31]. This approach represents a reasonable approximation for the mildly swirling jet flows studied in experiments [15], but it cannot provide an exact representation of instantaneous flow structures entering the jet flow region. Another problem related to the use of segregated RANS-LES models is the missing impact of the LES region on the RANS region. For high-swirl number flows, RANS models are known to be unreliable [28–30] so that inflow of uncertain accuracy is provided for the LES region if a segregated RANS-LES models is used.

The first goal of this paper is to address the questions described in the preceding paragraph and to extend our previous studies to the inclusion of the vortex breakdown

regime by using a unified RANS-LES model suggested by Heinz [32]. The unified RANS-LES model was applied to channel flow simulations so far to evaluate options regarding the computational realization of unified RANS-LES models and their cost and accuracy features [33]. The application to swirling turbulent jet flows reported here represents an application of this unified RANS-LES model to flows that require the use of hybrid RANS-LES methods. It is worth noting that the unified RANS-LES model will be applied 'as is', i.e., no attempt is made to adjust the model to the flows considered. The particular goal is to demonstrate the suitability of the unified RANS-LES model with respect to the flows considered.

The second goal is to show the difference between the unified RANS-LES model and other hybrid models. In addition to the consideration of our previously applied segregated RANS-LES model we focus here on a standard hybrid RANS-LES method: detached eddy simulation (DES) [34, 35]. Despite the success of DES when applied to massively separated flows, this simulation technique is known to suffer from non-trivial problems especially for internal flow applications. One of these problems is the 'modeled-stress depletion' (or 'gray area') problem. This problem appears if the DES model switches from RANS to LES, but the velocity fluctuations produced by LES are not sufficiently developed to compensate for the loss of modeled turbulent stresses [36, 37]. This problem is known to be relevant to jet-like flows [38, 39], such that DES calculations of swirling jet flows suffer from problems [40, 41]. Comparisons between the unified RANS-LES model to be applied here with DES and improved delayed detached eddy simulation (IDDES) [42], which was developed to significantly reduce this DES problem, will be beneficial to clarify, first, whether DES reveals the 'modeled-stress depletion' problem for the flows considered, and, second, whether the unified RANS-LES model [32] reveals such a problem.

The third goal of this paper is to use the results obtained to contribute to a better understanding of the structure of turbulent swirling jet flows. This concerns, in particular, the understanding of conditions for the onset and the organization of vortex breakdown.

The paper is organized in the following way. The adopted modeling approach is briefly described in Section 2. The computational approach is described in Section 3. Section 4 presents the results of validating the unified RANS-LES model, segregated RANS-LES, DES, and IDDES with available experimental data [15]. The differences between the computational methods considered regarding the simulation of swirling turbulent flows will be discussed in Sections 5–6 with respect to the prediction

of the onset of vortex breakdown and swirl effects on velocity and passive scalar fields. Conclusions of this study are presented in Section 7.

2 Unified RANS-LES model

The unified RANS-LES models derived by Heinz [32] by using stochastic analysis will be presented in the following. Incompressible flow will be considered, the compressible formulation can be found elsewhere [32]. The theoretical basis for the development of the hybrid RANS-LES models considered here is given by a realizable stochastic velocity model [32, 43–45]

$$\frac{dx_i^*}{dt} = U_i^*,\tag{1}$$

$$\frac{dU_i^*}{dt} = -\frac{1}{\rho}\frac{\partial \widetilde{p}}{\partial x_i} + 2\nu\frac{\partial \widetilde{S}_{ik}}{\partial x_k} - \frac{1}{\tau_L}\left(U_i^* - \widetilde{U}_i\right) + \sqrt{\frac{4c_0 k}{3\tau_L}}\frac{dW_i}{dt}.\tag{2}$$

Here, $x_i^*(t)$ and $U_i^*(t)$ represent the ith components of a fluid particle position and velocity, and d/dt refers to the derivative by time t. The first term on the right-hand side of eq. (2) represents the acceleration due to the pressure gradient and the second term represents the effect of the viscous forces: $\widetilde{S}_{ij} = (\partial\widetilde{U}_i/\partial x_j + \partial\widetilde{U}_j/\partial x_i)/2$ is the rate-of-strain tensor, $\widetilde{p}$ is the pressure, ρ is the constant mean mass density, and ν is the constant kinematic viscosity. The sum convention is used throughout this paper. Depending on the model formulation as RANS or LES model, $\widetilde{U}_i$ refers to the mean or filtered velocity (the filtering is defined as box filtering here). However, for simplicity, the model variables will be described as LES variables, this means we refer to the filtered velocity but keep in mind that this velocity can be the RANS velocity, too. The additional two terms in eq. (2) represent models for the relaxation and generation of subgrid-scale (SGS) velocity fluctuations, respectively. The third term describes a relaxation toward the filtered velocity $\widetilde{U}_i$ with a characteristic relaxation time scale τ_L. The generation of fluctuations is described by the noise term (the last term) which is determined by the properties of dW_i/dt. The latter is a Gaussian process with vanishing means, $< dW_i/dt >= 0$, and uncorrelated values at different times, $< dW_i/dt(t) \cdot dW_j/dt(t') >= \delta_{ij}\delta(t - t')$, where $\delta(t - t')$ refers to the delta function and δ_{ij} is the Kronecker symbol. k is the residual turbulent kinetic energy. The nondimensional parameter c_0 controls the noise strength.

The model (1) and (2) determines a transport equation for the filter density function (FDF) $F(w, x, t)$ of filtered velocities, where $w = (w_1, w_2, w_3)$ refers to the sample space velocity. The velocity FDF equation implied by eqs. (1) and (2) reads [32, 43]

$$\frac{\partial F}{\partial t} + \frac{\partial w_i F}{\partial x_i} = \frac{\partial}{\partial w_i}\left[\frac{1}{\rho}\frac{\partial \widetilde{p}}{\partial x_i} - 2\nu\frac{\partial \widetilde{S}_{ik}}{\partial x_k} + \frac{1}{\tau_L}\left(w_i - \widetilde{U}_i\right)\right]F$$
$$+ \frac{2c_0 k}{3\tau_L}\frac{\partial^2 F}{\partial w_i\partial w_i}.\tag{3}$$

By multiplying eq. (3) with 1 and w_i, respectively, and integrating over the velocity space, one finds that the stochastic model (1) and (2) reproduces exactly the continuity equation $\partial\widetilde{U}_k/\partial x_k = 0$ for incompressible fluids and the conservation of momentum equation

$$\frac{\widetilde{D}\widetilde{U}_i}{\widetilde{D}t} + \frac{\partial D_{ik}}{\partial x_k} = -\frac{1}{\rho}\frac{\partial \widetilde{p}}{\partial x_i} + 2\nu\frac{\partial \widetilde{S}_{ik}}{\partial x_k},\tag{4}$$

where $\widetilde{D}/\widetilde{D}t = \partial/\partial t + \widetilde{U}_k\partial/\partial x_k$ denotes the filtered Lagrangian time derivative. By multiplying eq. (3) with $w_i w_j$ and integrating over the velocity space, we can derive a transport equation for the SGS stress D_{ij}, which appears as an unknown in the momentum equation,

$$\frac{\widetilde{D}D_{ij}}{\widetilde{D}t} + \frac{\partial T_{kij}}{\partial x_k} = -D_{ik}\frac{\partial \widetilde{U}_j}{\partial x_k} - D_{jk}\frac{\partial \widetilde{U}_i}{\partial x_k} - \frac{2}{\tau_L}\left(D_{ij} - \frac{c_0}{3}D_{kk}\delta_{ij}\right).\tag{5}$$

Here, T_{ijk} is the triple correlation tensor of velocity fluctuations. For the following discussion it is helpful to rewrite eq. (5) for D_{ij} in terms of equations for the turbulent kinetic energy $k = D_{nn}/2$ and standardized anisotropy tensor $d_{ij} = (D_{ij} - 2k\delta_{ij}/3)/(2k)$. These equations are given by

$$\frac{\widetilde{D}k}{\widetilde{D}t} + \frac{1}{2}\frac{\partial T_{knn}}{\partial x_k} + 2kd_{kn}\frac{\partial \widetilde{U}_n}{\partial x_k} = -\frac{2(1 - c_0)k}{\tau_L},\tag{6}$$

$$\frac{\widetilde{D}d_{ij}}{\widetilde{D}t} + \frac{1}{2k}\frac{\partial(T_{kij} - T_{knn}\delta_{ij}/3)}{\partial x_k} + \frac{d_{ij}}{k}\frac{\widetilde{D}k}{\widetilde{D}t} + d_{ik}\frac{\partial \widetilde{U}_i}{\partial x_k}$$
$$- \frac{2}{3}d_{kn}\frac{\partial \widetilde{U}_n}{\partial x_k}\delta_{ij} = -\frac{2}{\tau_L}d_{ij} - \frac{2}{3}\widetilde{S}_{ij}.\tag{7}$$

The latter equations can be used to derive a consistent hierarchy of deterministic models. One possibility of using eqs. (4), (6), and (7) is to close these equations by a model for the triple correlation T_{ijk}, which is implied by the FDF transport equation considered [43, 46]. Another option, which will be considered in the following, is to reduce the computational effort significantly by using eq. (7) for the development of an algebraic model for the stress D_{ij}. Different algebraic stress models can be derived on the basis of an order of magnitude analysis involving a SGS Knudsen number [43]. The simplest model (a linear stress

model) is given by

$$D_{ij} = \frac{2}{3}k\delta_{ij} - 2\nu_t\widetilde{S}_{ij}, \tag{8}$$

where the turbulent viscosity ν_t is defined by $\nu_t = k\tau_L/3$. This model corresponds to neglecting the left-hand side terms in eq. (7), which results in $d_{ij} = -\widetilde{S}_{ij}\tau_L/3$. A better model (a quadratic stress model for D_{ij}) also reflects the stress production. This model corresponds to neglecting the transport terms (the first three terms) and using the linear model $d_{ij} = -\widetilde{S}_{ij}\tau_L/3$ to replace d_{ij} in the production terms on the left-hand side of eq. (7) [32]. However, such a quadratic stress model will be not considered here because the focus of this paper is on the analysis of basic properties of unified RANS-LES models. The combination of eq. (4) and $D_{ik} = 2k\delta_{ik}/3 - 2\nu_t\widetilde{S}_{ik}$ then results in

$$\frac{\widetilde{D}\widetilde{U}_i}{\widetilde{D}t} = -\frac{\partial(\widetilde{p}/\rho + 2k/3)}{\partial x_i} + 2\frac{\partial(\nu + \nu_t)\widetilde{S}_{ik}}{\partial x_k}. \tag{9}$$

The corresponding transport equation for k is given by

$$\frac{\widetilde{D}k}{\widetilde{D}t} = \frac{\partial}{\partial x_k}\left[(\nu + \nu_t)\frac{\partial k}{\partial x_k}\right] + \nu_t|\widetilde{S}|^2 - \frac{2(1-c_o)k}{\tau_L}, \tag{10}$$

where $|\widetilde{S}| = (2\widetilde{S}_{ij}\widetilde{S}_{ij})^{1/2}$. Equation (10) is obtained by using the stress model $D_{ik} = 2k\delta_{ik}/3 - 2\nu_t\widetilde{S}_{ik}$ in the production term and modeling the velocity triple correlation in the diffusion term [44, 45].

The setting of the time scale τ_L decides about the use of eqs. (9) and (10) combined with $\partial\widetilde{U}_k/\partial x_k = 0$ as LES or RANS equations: we apply LES equations if the LES time scale $\tau_L^{LES} = \ell_*\Delta/k^{1/2}$ is used, and RANS equations if the RANS time scale $\tau_L^{RANS} = \ell_*/\omega$ is applied. Here, $\Delta = (\Delta_x\Delta_y\Delta_z)^{1/3}$ refers to the filter width, ω is the turbulence frequency, and $\ell_* = 2(1-c_o)$ is a model parameter that is specified through the ω model. To close the RANS time scale $\tau_L^{RANS} = \ell_*/\omega$ we use the ω model of Bredberg et al. [47],

$$\begin{aligned}\frac{\widetilde{D}\omega}{\widetilde{D}t} =& C_{\omega 1}\frac{\omega}{k}\nu_t|\widetilde{S}|^2 - \frac{C_{\omega 2}}{C_k}\omega^2 + \frac{\partial}{\partial x_j}\left[(\nu + \frac{\nu_t}{\sigma_\omega})\frac{\partial\omega}{\partial x_j}\right] \\ &+ \frac{C_\omega}{k}(\nu + \nu_t)\frac{\partial k}{\partial x_j}\frac{\partial\omega}{\partial x_j}.\end{aligned} \tag{11}$$

Here, $C_{\omega 1}$, $C_{\omega 2}$, C_k, C_ω, and σ_ω are model constants that have the values $C_{\omega 1} = 0.49$, $C_{\omega 2} = 0.072$, $C_k = 0.09$, $C_\omega = 1.1$, and $\sigma_\omega = 1.8$. The comparison with the RANS limit $\nu_t^{RANS} = \ell_*k/(3\omega)$ of ν_t used in eqs. (10) and (11) with the RANS viscosity $\nu_t^{RANS} = C_kk/\omega$ used in the model of Bredberg et al. [47] reveals the consistency constraint $\ell_* = 3C_k$. The use of $C_k = 0.09$ corresponds to $\ell_* = 0.27$,

which is close to the standard value $\ell_* = 1/3$ for ℓ_* [43]. The value of ω at the first grid point is set to be $\omega = 2\nu/y^2$ [48]. The turbulent viscosity $\nu_t = k\tau_L/3$ derived above does not account for the damping effect of walls. This effect can be taken into account by using a modified turbulent viscosity $\nu_{t*} = f_\mu\nu_t$ [49]. For the damping function f_μ we use an expression applied in conjunction with the model of Bredberg et al. [47],

$$f_\mu = 0.09 + \left(0.91 + Re_t^{-3}\right)\left(1 - exp\left\{-\left(Re_t/25\right)^{2.75}\right\}\right). \tag{12}$$

Here, Re_t is the turbulence Reynolds number, which is defined by $Re_t = C_kk/(\omega\nu)$. The expression for f_μ ensures the correct scaling $O(y^3)$ of the turbulent viscosity in the near-wall RANS region: by using a Taylor series expansion [38, 47] we find $\nu_t \sim O(y^4)$ and $f_\mu \sim O(1/y)$.

The unification of RANS and LES equations can be achieved by introducing a unified time scale $\tau_L = min(\tau_L^{LES}, \tau_L^{RANS}) = \ell_*min(\Delta k^{-1/2}, \omega^{-1}) = \ell_*min(\Delta, L)/k^{1/2}$, where the characteristic length scale $L = k^{1/2}/\omega$ of turbulence is introduced. A more advanced coupling of RANS and LES equations is possible (the use of a smooth transfer function [32]), but channel flow simulations [33] and the simulations reported below did not indicate any advantage of such a model.

To visualize the flow structures of the different swirling jet flows considered below we add a passive scalar $\widetilde{\phi}$ to the flow field simulation. The transport equation for this scalar is given by

$$\frac{\widetilde{D}\widetilde{\phi}}{\widetilde{D}t} = \frac{\partial}{\partial x_k}\left[\left(\frac{\nu}{Sc} + \frac{\nu_t}{Sc_t}\right)\frac{\partial\widetilde{\phi}}{\partial x_k}\right]. \tag{13}$$

In consistency with our previous work [17] it is assumed that the Schmidt number Sc and turbulent Schmidt number Sc_t have the values $Sc = Sc_t = 1$. The turbulent viscosity is defined by $\nu_t = k\tau_L/3$.

At a first glance, there may be the impression that the unified RANS-LES model presented here is very similar to the $k - \omega$ SST-DES model suggested by Strelets [50] and Travin et al. [51], which is based on Menter's $k - \omega$ SST RANS model [52]. However, it turns out that there are significant differences between these models. First, the $k - \omega$ SST-DES model switches between the RANS and LES scales only in the dissipation term of the turbulent kinetic energy equation [50, 51, 53, 54], whereas the unified RANS-LES model switches these scales in all terms involving the unified time scale. Second, as a consequence of this DES concept applied, the $k - \omega$ SST-DES model does not recover commonly applied LES models in LES mode. Third, in contrast to the unified RANS-LES

model presented here, the $k - \omega$ SST-DES model is not part of a systematic hierarchy of turbulence models. Correspondingly, the SST-DES modeling approach does not provide a systematic basis for modeling improvements. On the other hand, the unified RANS-LES model considered can be improved by using, e.g., a nonlinear stress model (see the discussion following eqs. (8)) or a more advanced stochastic velocity model.

The performance of the unified RANS-LES model will be compared in following sections with the performance of other hybrid RANS-LES methods. First, the unified RANS-LES model results will be compared with the results of our previous segregated RANS-LES simulations [17]. The latter simulations were performed with FLUENT by using the dynamic Smagorinsky model (DSM) for performing LES in the jet region and the SST $k - \omega$ model [55] to perform RANS simulations in the nozzle region. In particular, we refer here to the forced LES segregated RANS-LES simulations where the forcing scheme of Smirnov et al. [31] is used to provide instantaneous inflow data for the LES jet flow simulations. In this way, the instantaneous inflow data are correlated such that the characteristic length and time scales of inflowing turbulent eddies are consistent with the corresponding RANS profiles imposed at the jet inlet. The specific purpose of the comparisons with our previous segregated RANS-LES simulations is to address the questions considered in Section 1. Second, for the $S = 0$ and $S = 0.23$ swirl cases for which experimental data are available for comparisons, the performance of the unified RANS-LES model will be compared with the performance of DES [34, 35] and IDDES [42] simulations, which were performed in addition to unified RANS-LES simulations. The standard DES and IDDES model constants are used, i.e., $C_{DES} = C_{IDDES} = 0.65$ and $C_w = 0.15$. The motivation of performing these simulations was to clarify whether DES and IDDES reveal the 'modeled-stress depletion' problem for the flows considered (see the discussion in the introduction), and to compare the performance of the unified RANS-LES model with commonly applied hybrid RANS-LES methods.

It is obvious that comparisons of our hybrid RANS-LES model with resolved LES would be interesting. First of all, this question is related to the resolution of the jet flow region, the motivation for including the nozzle flow calculation in our simulations is to provide realistic inflow data for the jet flow simulation. With respect to this question, it is relevant to note that our unified RANS-LES model is equivalent to resolved LES for most of the jet region with minor deviations close to the nozzle exit, see the discussion at the end of Section 3. To estimate the computational cost of a wall resolved LES we used simulation

results for the $S = 0.23$ case obtained with the unified RANS-LES model. Based on the averaged wall shear stress in the nozzle region with the smallest diameter (which is close to the nozzle exit) we found a friction velocity $u_\tau = 2.5\ m/s$ and a corresponding friction length scale $l_\nu = \nu/u_\tau = 7 \cdot 10^{-6}\ m$ (corresponding values for the other swirl cases do not differ much). The near wall resolution of the nozzle exit region is found to be $\Delta x^+ = \Delta x/l_\nu \approx 80$, $\Delta r^+ \approx 2$, and $\Delta r\theta^+ \approx 217$. The suggested resolution of wall resolved pipe flow LES is $\Delta x^+ \approx 40$, $\Delta r^+ \approx 1$ and $\Delta r\theta^+ = 15$ [56]. To achieve this suggested resolution, we would need a roughly 58 times finer grid. This is not feasible with the computational resources at our disposal. It appears to be likely that the majority of LES applications to similar flow configurations faces more or less the same problem.

3 Computational approach

The unified RANS-LES, DES and IDDES equations described in the preceding section were solved by using the OpenFOAM (Open Field Operation and Manipulation) CFD Toolbox [48]. The calculations have been performed using a finite-volume based method with the numerical grid being used as the LES filter. A filtered second-order central difference scheme was used for the discretization of the convection term in the velocity equations while a bounded second order central difference scheme has been employed for the convection terms in the $k - \omega$ equations to ensure a stable solution. With respect to the DES and IDDES simulations, the convection terms in the velocity and modeled viscosity equations have been discretized with a bounded second order central difference scheme to enable stable solutions. All the other terms were discretized using a second order central difference scheme. The PISO algorithm was used for the pressure-velocity coupling [57]. The resulting algebraic equation for all the flow variables except pressure has been solved iteratively using a preconditioned biconjugate gradient method with a diagonally incomplete LU preconditioning at each time step. The Poisson equation for pressure was solved by using an algebraic multigrid solver. When the residual became less than 10^{-5}, the algebraic equations were considered as converged. Time marching was performed by using a second-order backward difference scheme. The time step was modified dynamically to ensure a constant CFL number of 0.5.

The computational domain shown in Figure 1 consists of an upstream nozzle region and a downstream jet region. The jet region has a conical shape of radius D

Table 1: Domain discretization.

		Nozzle region	
Grid name	Grid points in the radial direction	Grid points in the axial direction	Grid points in the azimuthal direction
G1	wall region: 6; outer-wall region: 19	138	52
G2	wall region: 10; outer-wall region: 30	220	80
G3	wall region: 12; outer-wall region: 37	275	100
	Jet region		
Grid name	Grid points in the radial direction	Grid points in the axial direction	Grid points in the azimuthal direction
G1	37	50	52
G2	60	80	80
G3	75	100	100

and 2 D at the nozzle exit (which is the jet inlet) and the jet outlet, respectively. The picture shown in Figure 1 in the jet region shows the instantaneous scalar distribution of the $S = 0.23$ case. The standard grid G2 applied here divided the nozzle region into $700,000$ control volumes. To adequately resolve the near wall region, the grid was refined in the wall normal direction to ensure that $y^+ \leq 2.5$ at the first grid point. The G2 grid implied that the nozzle flow was simulated by LES with the exception of the near-wall region, which was treated as a RANS region. The jet region was discretized by using 80 points in the azimuthal direction (uniformly distributed), 60 points in the radial direction, and 80 points in axial direction with a stretching of 2%. The entire domain (nozzle and jet flow regions) was divided into $1,049,000$ control volumes. The details of the G2 domain dicretization are given in Table 1 and a close-up view of the mesh at the nozzle exit region is shown in Figure 2.

The simulations of nonswirling and swirling jet flows with swirl numbers S ranging from 0 to 1 were performed at a Reynolds number $Re = 10^5$. Here, Re is based on
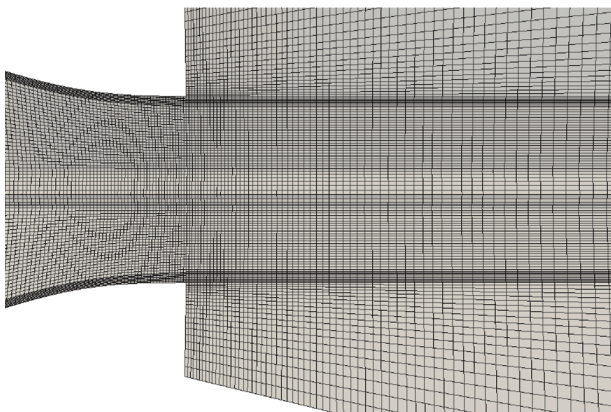
Figure 2: Close-up view of the G2 grid around the nozzle exit region.
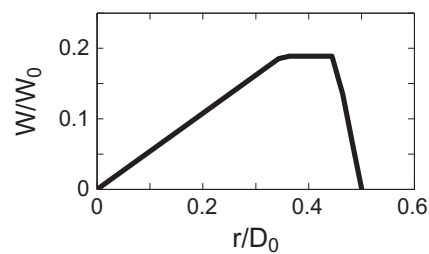
Figure 3: The nozzle inlet profile of the normalized azimuthal velocity W for the swirl case $S = 0.23$. The normalization data are $W_0 = 21.7 \, m/s$ and $D_0 = 0.248 \, m$.

the radially averaged axial velocity at the nozzle exit and the nozzle diameter $D = 0.0381 \, m$. The swirl number S is defined by [15, 17, 58]

$$S = \frac{2 \int_0^{D/2} r^2 U W dr}{D \int_0^{D/2} r U^2 dr}. \tag{14}$$

U and W are the averaged filtered axial and azimuthal velocity components, respectively, and r is the radial position. The relation between S and the swirl number S_1 defined by the replacement of U^2 by $U^2 - W^2/2$ in the denominator of eq. (14) is given by $S = (3.9 S_1 / [1 + 4.1 S_1])^2$ [17].

The boundary conditions required to simulate these cases were specified in the following way. A uniform value of the axial velocity $U = 1.17 \, m/s$ at the nozzle inlet was used for all swirl cases. For the $S = 0.23$ swirl case a profile of the azimuthal velocity was applied which can be seen in Figure 3. The corresponding azimuthal velocity profiles for the other swirl cases considered were obtained by a rescaling of the $S = 0.23$ profile: the latter was multiplied with $(2.25, 2.7, 3.15, 4.2, 6.8)$ for the $S = (0.5, 0.55, 0.6, 0.75, 1)$ cases considered, respectively. The settings for axial and azimuthal velocities were combined with a zero radial velocity at the nozzle inlet. A no-slip boundary condition

Table 2: Boundary conditions for unified RANS-LES and DES simulations.

Boundary	Variables	Settings
Nozzle inlet	Velocity field:	
	$S = 0$: (U,V,W)	(1.17, 0, 0) m/s
	$S = 0.23$: (U,V,W)	(1.17,0,W: see Figure 3) m/s
	SGS kinetic energy k	0.003 m^2/s^2
	Specific dissipation rate ω	0.53 $1/s$
	Pressure	Zero gradient
	Scalar	1.0
	DES $\tilde{\nu}$	$1.5 \cdot 10^{-5}$ m^2/s
Wall	Velocity field	No slip condition
	Turbulent kinetic energy k	No slip condition
	Specific dissipation rate ω	Zero gradient
	Pressure	Zero gradient
	Scalar	Zero gradient
	DES $\tilde{\nu}$	0 m^2/s
Annulus	Velocity field	pressure inlet [48]
	SGS kinetic energy k	10^{-11} m^2/s^2
	Specific dissipation rate ω	Zero gradient
	Pressure	Atmospheric pressure
	Scalar	Zero gradient
	DES $\tilde{\nu}$	$1.5 \cdot 10^{-5}$ m^2/s
Far-field boundary	Velocity field	pressure inlet [48]
	SGS kinetic energy k	10^{-11} m^2/s^2
	Specific dissipation rate ω	Zero gradient
	Pressure	Atmospheric pressure
	Scalar	Zero gradient
	DES $\tilde{\nu}$	$1.5 \cdot 10^{-5}$ m^2/s
Outlet	Velocity field	pressure inlet [48]
	SGS kinetic energy k	Zero gradient
	Specific dissipation rate ω	Zero gradient
	Pressure	Atmospheric pressure
	Scalar	Zero gradient
	DES $\tilde{\nu}$	Zero gradient

was used for the velocity at the wall. At the far-field boundary and the jet outlet boundary a fixed atmospheric pressure was set for the pressure and the velocity was specified depending on whether the flow is out of the boundary (zero normal gradient) or into the domain (zero azimuthal velocity component, normal component obtained from known flux). Details of the boundary conditions applied can be found in Table 2. Additional evidence for the validity of these boundary conditions can be found in Zemtsop et al. [17].

The simulations were performed for 60 large eddy turnover times $t_e = D/U_0$ to eliminate the effect of the initial conditions. Here, U_0 is the maximum axial velocity at the nozzle exit. The large eddy turnover time t_e was calculated for the $S = 0.23$ case. After this time, the simulations were run for 1500 large eddy turnover times to collect time statistics. Due to the axi-symmetry of the flows considered, an additional averaging of the time statistics over the azimuthal direction has been performed. All averages

shown in this paper have been obtained in this way. The suitability of these simulation time settings was proven in our previous studies [17].

The suitability of the domain size considered is addressed in terms of Figure 4, which shows the mean axial velocity and normalized intensity u' of axial velocity fluctuations along the centerline for the $S = 0.23$ and $S = 0.6$ cases ($S = 0.6$ is the first case for which vortex breakdown was observed). In particular, this figure shows the difference between using the domain size applied for all the other simulations, which is referred to as small domain, and the use of a larger domain size, which is referred to as large domain. The latter domain was obtained by an axial extension of the jet domain from $4.2D$ to $8D$, and a radial extension at the outlet from $4D$ to $6.5D$. The comparison for $S = 0.23$ shows almost the same result for both domain sizes. With respect to $S = 0.6$, it may be seen that both solutions are almost identical throughout the nozzle and the vortex breakdown (flow reversal)
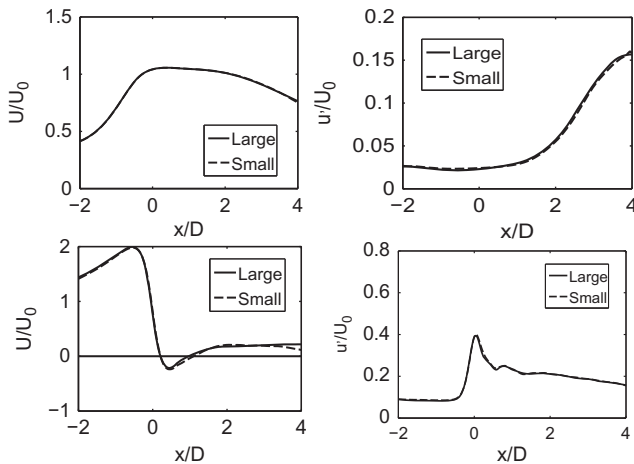
Figure 4: The large domain effect. The normalized mean axial velocity and normalized intensity u' of axial velocity fluctuations along the centerline for the $S = 0.23$ (first row) and $S = 0.6$ (second row) case.

Figure 5: The grid influence on $S = 0.23$ results: Radial distributions of the normalized averaged azimuthal velocity W at different x/D obtained by the unified model. Dotted line: G3 grid; solid line: G2 grid; dashed line: G1 grid; dots: measurements. Here, $W_0 = 21.7 \, m/s$.

region. A small difference of streamwise velocities can be observed close to the outlet of the small domain. However, the main observation is that the vortex breakdown simulation is not affected by the domain size. Thus, the use of the small domain is well appropriate.

The suitability of the G2 grid applied for the following simulations was proven in the following way. Regarding the jet region, the G2 grid applied is equal to the grid applied in our previous segregated RANS-LES simulations [17]. Regarding the nozzle region, the G2 grid (704,000 grid points) consists of more points than the grid applied in our previous segregated RANS-LES simulations (78,000 grid points) because it is a three-dimensional grid whereas the segregated RANS-LES simulations adopted a two-dimensional grid in the nozzle. The suitability of the grid applied in our previous segregated RANS-LES simulations was shown by detailed grid dependence studies [17]. Therefore, it can be expected that the G2 grid applied here is well appropriate. This view was confirmed by grid dependence studies performed on three grids: 270,000 (G1), 1.05 million (G2), and 2 million (G3) grid points, respectively. The number of grid points in the axial, radial, and azimuthal directions were uniformly increased from G1 to G2 and G3 by using refinement factors of 1.25^2 and 1.25^3, respectively, in each of the three space directions. The number of grid points in each direction is given in Table 1 for each mesh. Figure 5 shows the corresponding plots of the mean azimuthal velocity at the nozzle exit and two downstream locations for the three grids considered in comparison to Gilchrist and Naughton's [15] experimental data. It can be seen that the profile of the azimuthal velocity predicted by simulations using the G2 and
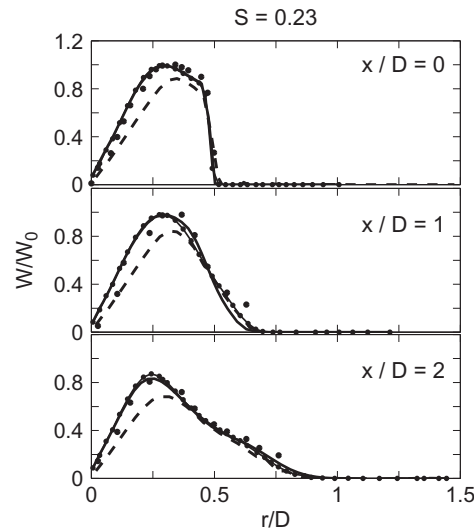
G3 grids agree very well with the experimental data. On the other hand, the G1 grid results underpredict the experimental data significantly, leading to the conclusion that the G1 grid is not well appropriate for the studies reported below. Hence, all further results are presented on the G2 grid which enables much more efficient simulations than the use of the G3 grid.

The question of the dominance of RANS and LES modes is addressed in terms of Figures 6 and 7 that show the ratio k_{res}/k_{tot} of resolved to total turbulent kinetic energy obtained from the unified RANS-LES model at several axial locations within the nozzle (Figure 6) and within the jet region (Figure 7). The resolved turbulent kinetic energy is calculated using a time average $k_{res} = (\langle \widetilde{U}_i \widetilde{U}_i \rangle_{TA} - \langle \widetilde{U}_i \rangle_{TA} \langle \widetilde{U}_i \rangle_{TA})/2$, the modeled turbulent kinetic energy is obtained as a time average of the solution of eq. (6), $k_{mod} = \langle k \rangle_{TA}$, and the total turbulent kinetic energy is given by $k_{tot} = k_{res} + k_{mod}$. Here, the subscript TA refers to time averaged variables. A main novelty of the work presented here is the inclusion of the flow through the (wall bounded) nozzle region upstream of the jet region (free shear flow). The adopted grid is too coarse to fully resolve the near wall turbulent motions and thus the use of a hybrid RANS-LES model is crucial to accurately model the flow through the nozzle and to provide accurate inflow into the jet region. Ideally, the unified hybrid RANS-LES model operates in unsteady RANS mode close to the wall in the nozzle and mostly in LES mode in the jet flow. The ratio k_{res}/k_{tot} is a good measure to identify which mode dominates. LES is often considered to be characterized by $k_{res}/k_{tot} \geq 0.8$
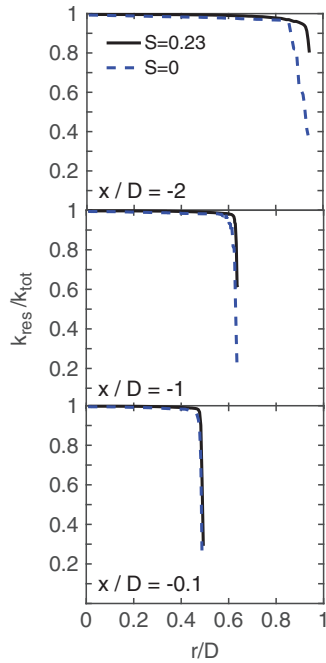
Figure 6: The ratio of resolved to total turbulent kinetic energy obtained from the unified RANS-LES model for $S = (0, 0.23)$ at different axial positions within the nozzle.
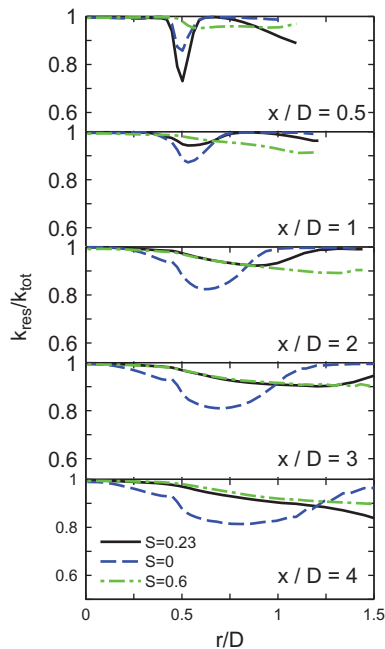
Figure 7: The ratio of resolved to total turbulent kinetic energy obtained from the unified RANS-LES model for $S = (0, 0.23, 0.6)$ at different axial positions within the jet region.

[49], whereas in unsteady RANS $k_{res}/k_{tot} < 0.4$ is typical. Indeed, Figure 6 shows $k_{res}/k_{tot} < 0.3$ close to the nozzle exit where the Reynolds number is the largest and thus the

modeled contribution is up to 70%. This clearly demonstrates that the unified model operates as a unsteady RANS model in the near wall region. Figure 7 shows the ratio in the jet region. It can be seen that $k_{res}/k_{tot} \geq 0.8$ almost everywhere except in the thin shear layer close to the nozzle exit ($x/D = 0.5$) where $k_{res}/k_{tot} \approx 0.7$ is found for the non-swirling jet ($S = 0$), indicating slightly less resolved LES. The unified RANS-LES model results can thus be considered to be LES in the jet region.

4 Hybrid RANS-LES model evaluation

Next, the performance of the unified RANS-LES model will be validated by using Gilchrist and Naughton's [15] experimental data, which are only available for the nonswirling $S = 0$ case and the mild swirl $S = 0.23$ case. The simulations were adjusted to the same conditions (including the Reynolds number $Re = 10^5$) as considered in Gilchrist and Naughton's [15] experiments. The results discussed in this section will be compared with the results of our previous segregated RANS-LES FLUENT simulations: see Figures 3, 7–9 in reference [17]. In addition, we will also compare our simulation results with the results of our DES and IDDES simulations (see the discussion of these simulations at the end of this section).

Mean velocities at the nozzle exit ($x/D = 0$), which were obtained by unified RANS-LES, DES, IDDES, and experiments, are shown in Figure 8 for the nonswirling ($S = 0$) and swirling case ($S = 0.23$). Only the resolved turbulence intensities are shown because the subgrid-scale (SGS) turbulence intensities are small compared to the resolved intensities in the regions used for comparisons with experimental results. The mean velocity comparisons in Figure 8 show an excellent performance of all models. Only a small difference between the three models can be observed: the azimuthal velocity is predicted slightly better by the unified RANS-LES model. A comparison of turbulence intensities is given in Figure 9. For the non-swirling case the unified RANS-LES model predicts sufficiently large velocity fluctuations. The sharp peak of axial velocity fluctuations (which is produced in the boundary layer) has not been measured due to a lack of resolution in the radial locations where hot-wire measurements have been taken. In contradiction with the measurements, the DES and IDDES results show much smaller levels of fluctuations. The RANS region close to the nozzle wall is too dominant in the DES and IDDES simulations, which prevents the generation of velocity fluctuations in the LES
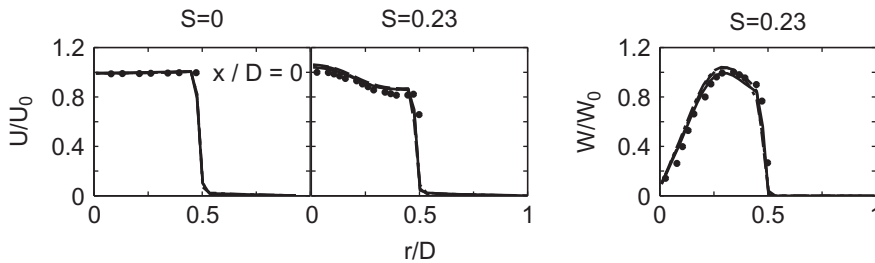
Figure 8: Unified RANS-LES results at the nozzle exit $x/D = 0$: Radial distributions of normalized averaged axial and azimuthal velocity components U and W, respectively, for $S = 0$ and $S = 0.23$. Solid line: unified RANS-LES model; dot-dashed line: DES; dashed line: IDDES; dots: experimental data. The normalization data are $U_0 = 50.4\ m/s$ for the nonswirling case and $U_0 = 56.3\ m/s$, $W_0 = 21.7\ m/s$ for the swirling case.
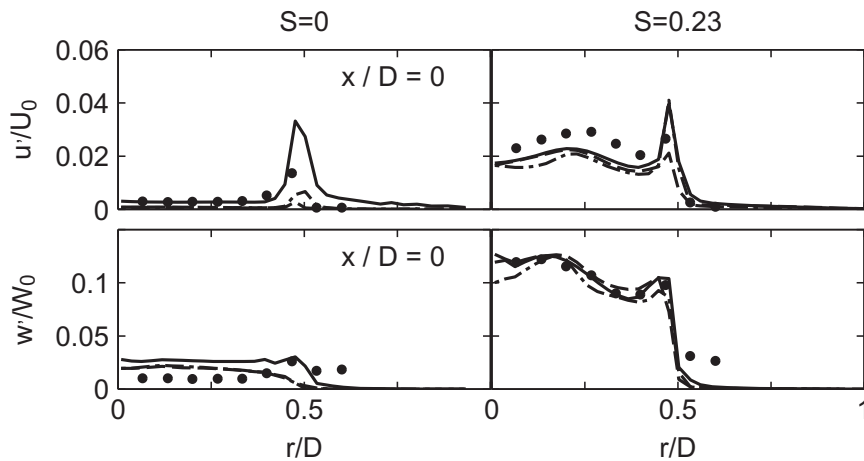
Figure 9: Unified RANS-LES results at the nozzle exit $x/D = 0$: Radial distributions of normalized intensities u' of axial velocity fluctuations and normalized intensities w' of azimuthal velocity fluctuations for $S = 0$ and $S = 0.23$. Solid line: unified RANS-LES model; dot-dashed line: DES; dashed line: IDDES; dots: experimental data.

region of the nozzle: see the 'modeled-stress depletion' problem described in the introduction [36, 37]. The lack of velocity fluctuations at the nozzle exit has significant consequences for the development of the jet further downstream, as will be discussed below. For the swirling case (left two plots in Figure 9), all models predicted very similar amounts of velocity fluctuations in agreement with the measurements. The flow instability and turbulence production mechanisms of the swirling case seem to be sufficiently strong to trigger velocity fluctuations in all three models considered. We may conclude that the unified RANS-LES model predicts the mean jet inflow more accurately than the other considered models with regard to both the nonswirling and swirling case. The unified RANS-LES results obtained here agree nicely with recent RANS predictions of mean velocities at the nozzle exit, which were obtained by using the segregated RANS-LES model [17]. Turbulence intensities were not reported in reference [17].

Mean velocities in the jet region, which were obtained by unified RANS-LES simulations and experiments, are shown in Figure 10 for the nonswirling ($S = 0$) and swirling case ($S = 0.23$) at four downstream locations $x/D = 1, 2, 3, 4$. The mean velocities obtained from the unified RANS-LES model agree very well with the experimental data for both the nonswirling and swirling cases at all downstream locations. It may be seen that axial and azimuthal velocities are characterized by different mixing length scales: the azimuthal velocity decays more rapidly than the axial velocity, as may be seen by comparing the peak values of U and W at $x/D = 1$ and $x/D = 4$. Two-equation turbulence models are unable to correctly simulate the different mixing of axial and azimuthal velocities [28], whereas the unified RANS-LES model enables a correct simulation of the different mixing of axial and azimuthal velocities. The unified RANS-LES model results agree better with the experimental results than results obtained recently by using a segregated RANS-LES model
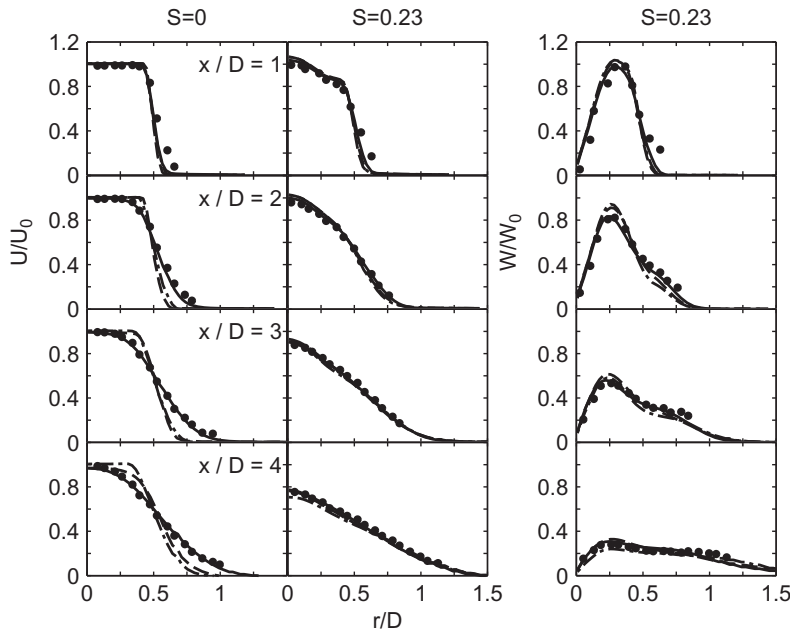
Figure 10: Unified RANS-LES results in the jet region: Radial distributions of the normalized averaged axial and azimuthal velocity components U and W, respectively, for $S = 0$ and $S = 0.23$ at different axial positions x/D. Solid line: unified RANS-LES model; dot-dashed line: DES; dashed line: IDDES; dots: experimental data.
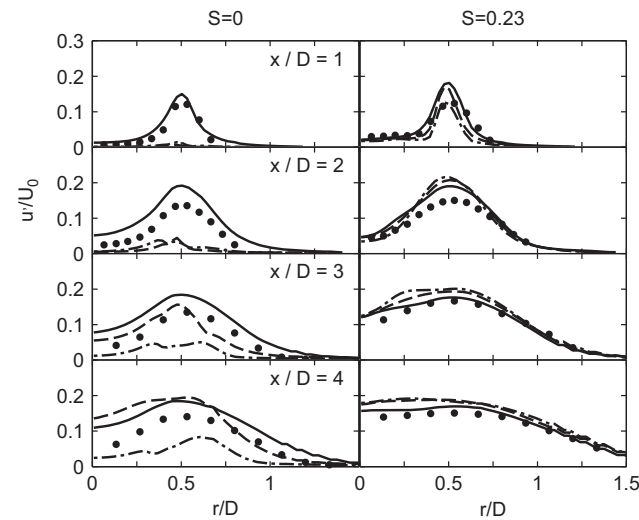
Figure 11: Unified RANS-LES results in the jet region: Radial distributions of normalized intensities u' of axial velocity fluctuations for $S = 0$ and $S = 0.23$ at different axial positions x/D. Solid line: unified RANS-LES model; dot-dashed line: DES; dashed line: IDDES; dots: experimental data.
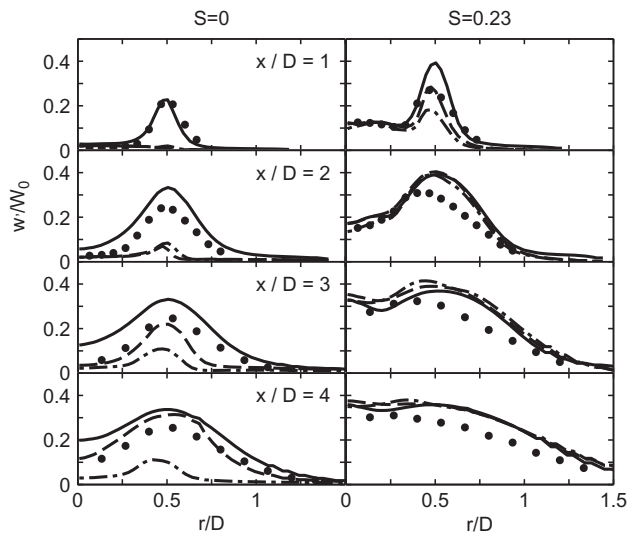
Figure 12: Unified RANS-LES results in the jet region: Radial distributions of normalized intensities w' of azimuthal velocity fluctuations for $S = 0$ and $S = 0.23$ at different axial positions x/D. Solid line: unified RANS-LES model; dot-dashed line: DES; dashed line: IDDES; dots: experimental data.

[17]. This applies, in particular, to the azimuthal velocity, which is slightly underpredicted by the segregated RANS-LES model. Both the DES and IDDES results show a very good agreement with the experimental results for the swirling $S = 0.23$ case. However, the DES and IDDES results for the nonswirling case reveal shortcomings: the jet expansion is significantly underpredicted.

Resolved turbulence intensities in the jet region, which were obtained by unified RANS-LES simulations and experiments, are shown in Figures 11-12 for the nonswirling ($S = 0$) and swirling case ($S = 0.23$) at four downstream locations $x/D = 1, 2, 3, 4$. The turbulence intensities obtained from the unified RANS-LES model agree well with the experimental data for both the nonswirling and

swirling cases. Compared to the experimental data, we observe slight overpredictions of the unified RANS-LES model predictions. Similar overpredictions were reported recently in studies based on a segregated RANS-LES model [17]. For the swirling case $S = 0.23$, the DES and IDDES predictions of axial and azimuthal velocity fluctuations compare well with the unified RANS-LES results. The corresponding DES predictions for the nonswirling case are incorrect, in particular for $x/D = 1, 2$. The reason for the unsatisfactory performance of DES is the lack of velocity fluctuations at the nozzle exit: see Figure 9. IDDES, which was developed to significantly reduce this DES problem [42], suffers from the 'modeled-stress depletion' problem in the same way as DES for about half of the computational domain: see the $x/D = 1, 2$ pictures. With growing distance from the nozzle exit, IDDES recovers from the 'modeled-stress depletion' problem and provides results which are comparable to the unified RANS-LES results: see the $x/D = 3, 4$ pictures. However, this recovery of the IDDES performance is not much reflected in the mean axial velocity profiles at $x/D = 3, 4$ which underpredict the jet expansion significantly. This leads, for example, to incorrect scalar mixing predictions. Therefore, the performance of both DES and IDDES is unsatisfactory with respect to the nonswirling case. It is interesting to note that the addition of swirl leads to a significant enhancement of the production of LES fluctuations such that the performance of DES and IDDES with respect to swirling flows is comparable to the performance of the unified RANS-LES model.

The DES results described above were obtained by using the typical DES filter width definition $\Delta = \max(\Delta_x, \Delta_y, \Delta_z)$. The comparison with the unified RANS-LES model, which uses $\Delta = (\Delta_x \Delta_y \Delta_z)^{1/3}$, leads then to the question of what is the difference if DES is used in conjunction with $\Delta = (\Delta_x \Delta_y \Delta_z)^{1/3}$. The latter question is addressed in terms of Figure 13, which shows the mean axial velocity and the normalized intensity of axial velocity fluctuations for the $S = 0$ case for both $\Delta = \max(\Delta_x, \Delta_y, \Delta_z)$ and $\Delta = (\Delta_x \Delta_y \Delta_z)^{1/3}$. It may be seen that the use of $\Delta = (\Delta_x \Delta_y \Delta_z)^{1/3}$ definitely improves the velocity and turbulence simulations. However, compared to unified RANS-LES results, the DES approach still reveals significant shortcomings. First, at $x/D = 1$, the characteristic 'modeled-stress depletion' problem of DES is seen. Second, farther away from the nozzle, we see a strong overprediction of the intensity of axial velocity fluctuations in the jet center region. The differences between using $\Delta = \max(\Delta_x, \Delta_y, \Delta_z)$ and $\Delta = (\Delta_x \Delta_y \Delta_z)^{1/3}$ can be attributed to the eddy viscosity, which is smaller if $\Delta = (\Delta_x \Delta_y \Delta_z)^{1/3}$ is used. A smaller eddy viscosity will result in the generation of additional LES fluctuations. This may
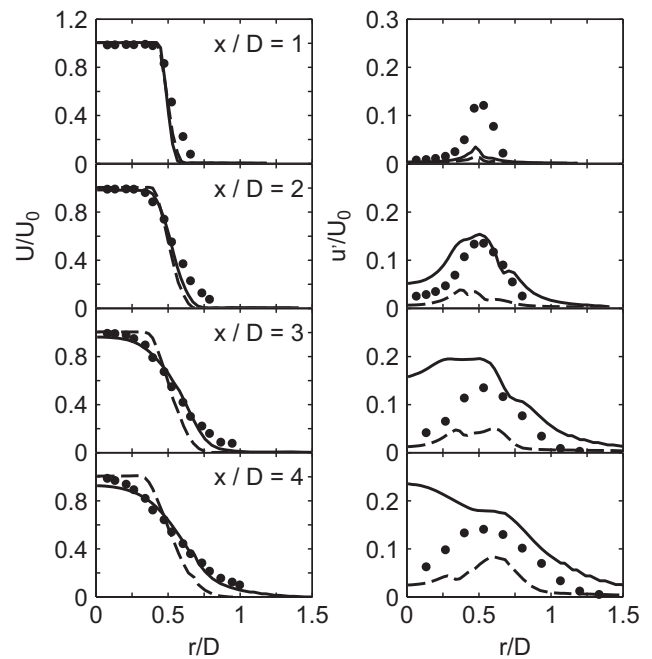
Figure 13: DES results in the jet region: Radial distributions of the normalized averaged axial velocity U and normalized intensities u' of axial velocity fluctuations for $S = 0$ at different axial positions x/D. Solid line: $\Delta = (\Delta_x \Delta_y \Delta_z)^{1/3}$; dashed line: $\Delta = \max(\Delta_x, \Delta_y, \Delta_z)$; dots: experimental data.

have a positive effect as seen at $x/D = 1$, but it can also imply unrealistic negative effects, as seen by the huge overprediction of fluctuations in the jet core region. In an attempt to better understand the difference between the unified RANS-LES and the $k - \omega$ SST DES concepts we performed (by using $\Delta = (\Delta_x \Delta_y \Delta_z)^{1/3}$) simulations with the unified RANS-LES model, where the RANS-LES time scale switch was only applied in the dissipation term of the turbulent kinetic energy equation (this means the RANS time scale was used in all the other terms). These simulations resulted in mean axial velocity fields which have shortcomings (an underprediction of the jet expansion was seen). However, the most relevant shortcoming was the almost complete lack of LES fluctuations (not shown). This finding also supports the view that the DES concept results in a significant sensitivity of the generation of fluctuations depending on variations of the turbulence model, definition of Δ, and grid applied.

5 Vortex breakdown

At swirl numbers larger than $S = 0.23$ the flow structures may drastically change. Centrifugal forces can significantly reduce the centerline pressure close to the nozzle,

whereas the pressure on the swirl-axis farther away from the nozzle is much less affected (i.e., much higher than the pressure close to the nozzle due to the reduced swirl velocity). The latter can be seen, e.g., in terms of the pressure distributions presented in reference [17]. This results in an adverse pressure gradient in axial direction. The flow is decelerated and (depending on the swirl strength) eventually reversed, creating a semi-stable recirculation zone (i.e., vortex breakdown) [20]. A crucial question is whether the unified RANS-LES model predicts vortex breakdown in agreement with other observations. This question will be addressed now on the basis of the vortex breakdown criterion of Billant et al. [59] and observations made in experiments [2, 4, 6, 20, 21, 60–62].

Mathematically, the onset of vortex breakdown can be described in the following way. According to Bernoulli's principle the sum of P/ρ and the kinetic energy is constant along the centerline (P refers to the mean pressure). Therefore, for the flow considered where the mean streamline velocity U clearly dominates the kinetic energy we find that $P/\rho + U^2/2$ is constant along the centerline. Hence, we have $P_0/\rho + U_0^2/2 = P_1/\rho + U_1^2/2$. Here, the subscript 0 refers to values of P and U at a reference position x_0 at the centerline located well upstream of the stagnation point, and the subscript 1 refers to the stagnation point. The streamwise velocity U_1 at the stagnation point can be assumed to be negligibly small compared to the pressure contribution. Therefore, the condition to observe vortex breakdown is given by

$$\frac{P_1 - P_0}{\rho} = \frac{U_0^2}{2}. \tag{15}$$

According to eq. (15), vortex breakdown occurs if the pressure difference divided by ρ between the stagnation point and reference position x_0 becomes equal to the specific kinetic energy at the reference position. However, the use of the criterion eq. (15) for the prediction of the onset of vortex breakdown is difficult because the intensity of swirl needed to observe vortex breakdown is only implicitly involved via the pressure difference. A more helpful criterion can be obtained by the following approach. Billant et al. [59] consider the balance between the radial pressure gradient and centrifugal force far upstream of the stagnation point for laminar flow. Integrated over the radial direction, this balance implies

$$\frac{P_\infty - P_0}{\rho} = \int_0^\infty \frac{W^2(r, x_0)}{r} dr. \tag{16}$$

We take the difference between eqs. (16) and (15) to obtain

$$\frac{P_\infty - P_1}{\rho} = \int_0^\infty \frac{W^2(r, x_0)}{r} dr - \frac{U_0^2}{2}. \tag{17}$$

By introducing the abbreviations

$$R_P = 2\frac{P_\infty - P_1}{\rho U_0^2}, \qquad R = \frac{2}{U_0^2} \int_0^\infty \frac{W^2(r, x_0)}{r} dr, \tag{18}$$

eq. (17) reads

$$R_P = R - 1. \tag{19}$$

Both R_P and R are positive: see eq. (16) considered at the stagnation point and the definition of R. For the case that the stagnant region is directly connected to the surrounding outer quiescent fluid, Billant et al. [59] argue that $P_\infty = P_1$ represents a good approximation. The corresponding condition for the onset of vortex breakdown is then $R = 1$. In the case of a bubble state as considered here, the stagnant region is not directly connected to the surrounding outer quiescent fluid, which implies that $P_\infty \geq P_1$. For this case, a necessary condition for the onset of vortex breakdown is $R \geq 1$ [59]. Hence, vortex breakdown can be observed if the specific kinetic energy at the reference position x_0 is smaller than the rotational energy.

Unified RANS-LES simulations on the G2 grid were used to calculate R for different swirl numbers. The reference point $x_0 = 0$ was chosen. These simulations resulted in $R = (0, 0.330, 0.919, 1.116, 1.619)$ for $S = (0, 0.23, 0.50, 0.55, 0.60)$. Figure 14 shows the plot of R values in comparison to the model function

$$R = 1.1114S + (1.1857S)^2 + (1.6019S)^{20}. \tag{20}$$

This curve fit was obtained by calculating (for fixed powers in the second and third terms) the coefficients of
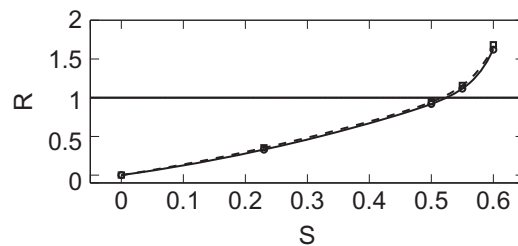
Figure 14: Vortex breakdown criterion: The dependence of the rotational-to-kinetic energy ratios R and R_t on the swirl number S for $S \leq 0.6$. The dots and the solid line, which shows eq. (20), show the results for R. The rectangles and the dashed line, which shows eq. (21), show the results for R_t.

S in all three terms such that the curve agrees exactly with the R values at $S = (0.23, 0.50, 0.55)$. A quadratic second term was applied, and the power of the last term was chosen such that the R value at $S = 0.6$ is provided. The curve fit eq. (20) can be used to determine under which condition the vortex breakdown criterion $R \geq 1$ is satisfied: we find that vortex breakdown may occur if $S \geq 0.5244$. In an attempt to improve the vortex breakdown condition $R \geq 1$, the analysis of Billant et al. [59] was repeated by including the effect of turbulence. This approach results in the replacement of W^2 by $W^2 + w'^2$ in R, where w'^2 refers to the azimuthal turbulence intensity. For this case we found $R_t = (0, 0.353, 0.945, 1.157, 1.665)$ for $S = (0, 0.23, 0.50, 0.55, 0.60)$, respectively. The corresponding curve fit for this case, which was obtained like eq. (20), is given by

$$R_t = 1.2691S + (1.0747S)^2 + (1.5964S)^{17}. \tag{21}$$

As shown in Figure 14, the effect of this modification of the vortex breakdown criterion is negligibly small.

The unified RANS-LES simulations did not show vortex breakdown for $S = (0, 0.23, 0.50, 0.55)$. Vortex breakdown was found for $S = 0.6$ and higher swirl numbers. Evidence for the observation of vortex breakdown for $S \geq 0.6$ is provided in terms of Figure 15, which also shows that vortex breakdown was observed in the jet region just outside of the nozzle for all the swirl cases considered. The latter fact is also confirmed in terms of Figure 16, which shows a contour plot of the normalized instantaneous axial velocity in the center-plane $x_3 = 0$ for the strongest swirl case $S = 1$ considered. The finding of vortex breakdown for $S = 0.6$ is consistent with the implication of the vortex breakdown criterion: $S \geq 0.52$ is a necessary condition but not a sufficient condition to observe vortex breakdown. The fact that vortex breakdown is observed for a swirl number slightly higher than $S = 0.52$ supports the view that the vortex breakdown
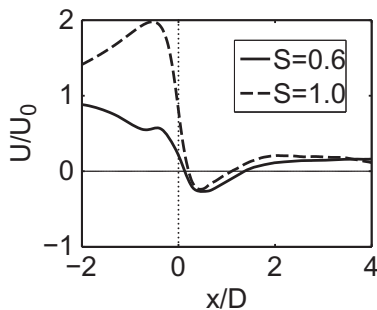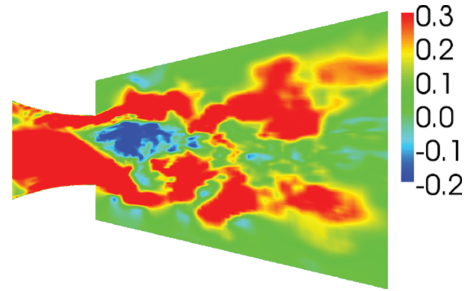
Figure 16: Unified RANS-LES results for $S = 1$: Contour plot of the normalized instantaneous axial velocity in the center-plane $x_3 = 0$.

condition provides valuable information about the onset of vortex breakdown. The observation that vortex breakdown is found for the considered jet flow at $S = 0.6$ is well supported by conclusions of experiments: a critical swirl number of $S = 0.6$ for the onset of breakdown is well accepted [2, 4, 6, 20, 21, 60–62]. DES and IDDES simulations performed at $S = 0.6$ (not shown) also resulted in the observation of vortex breakdown. Thus, the unified RANS-LES simulation results agree very well with observations made by theory, experiments, and other computations.

The detailed mechanism of vortex breakdown is currently not fully understood [6, 63]. Experiments [6, 63, 64] indicate that swirl flows are characterized by a central vortex core, which shows a characteristic precession in swirl flows involving vortex breakdown (called precessing vortex core (PVC)). The central vortex core can be seen in the flow visualization of Figure 17 which shows iso-surfaces $\tilde{p} - P = -20\,Pa$ of instantaneous pressure fluctuations obtained with the unified RANS-LES model for swirl numbers $S = (0, 0.23, 0.50, 0.75, 1)$. The iso-surface is colored according to the filtered scalar value. The way of visualizing instantaneous flow structures follows our presentation in reference [17]. This approach has significant advantages compared to the consideration of instantaneous vorticity fields, which does not allow to visualize the coherent flow structures in swirling jets [17, 24]. The nonswirling case (right) does not have a vortex core. The $S = (0.75, 1)$ cases (two leftmost pictures) with vortex breakdown also seem to indicate a PVC as the axis of the vortex core in these two pictures displays an angle to the symmetry axis.

A much stronger indication for the existence of the PVC can be found by analyzing the power spectral density of velocity fluctuations [24] as shown in Figure 18. This figure shows the axial velocity fluctuation power spectral density obtained from the unified RANS-LES model for $S = 0.55$, for which we do not observe vortex breakdown, and for $S = 0.6$, for which we observe vortex breakdown. The velocity spectrum calculations were performed in the

Figure 15: The mean axial velocity along the centerline. Solid line: $S = 0.6$; dashed line: $S = 1$.
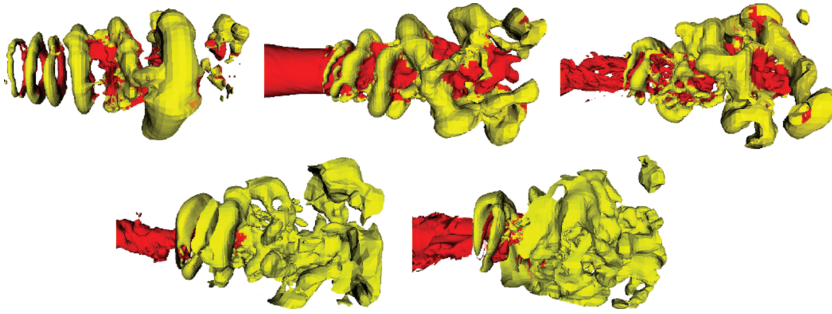
Figure 17: Unified RANS-LES results: Visualization of coherent vortex structures by means of an iso-surface $\widetilde{p} - P = -20\ Pa$ of instantaneous pressure fluctuations for swirl numbers $S = (0, 0.23, 0.5, 0.75, 1)$ from left to right, respectively. The iso-surface is colored according to the scalar value: $\widetilde{\phi} \geq 0.5$ (red) and $\widetilde{\phi} < 0.5$ (yellow).
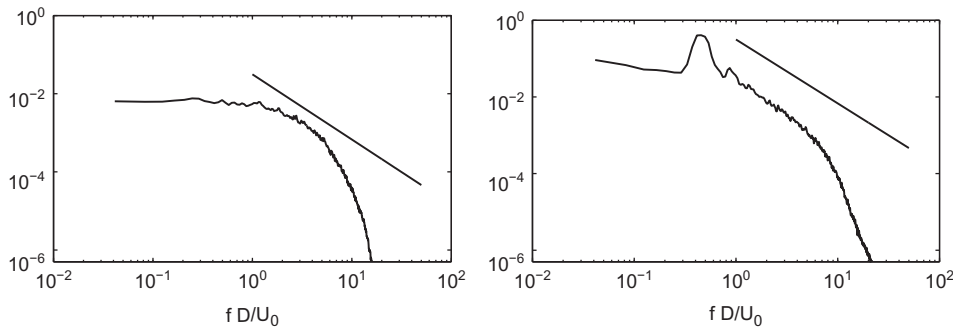
Figure 18: Power spectral density of axial velocity fluctuations at $x/D = 0.1$ and $r/D = 0.6$. Left-hand side: $S = 0.55$, right-hand side: $S = 0.6$. The straight line has a slope of -5/3.

following way [24]. Time signals of velocity have been recorded during the simulation close to the nozzle exit at $x/D = 0.1$ and $r/D = 0.6$ at twelve angular positions. The signal was recorded every other time step for a total of 86 turnover times giving a total of 30,000 samples. The power spectral density of axial velocity fluctuations was calculated by using a windowed Fourier transform with a Hanning window using 5 overlapping segments. This is done for each of the angular positions. Then, additional averaging of the spectra over the twelve locations was applied. There are two remarkable differences between these two swirl cases. First, the $S = 0.6$ case shows much higher levels of power density at low frequencies and a region where the spectrum decays with a $-5/3$ slope over about one decade in frequency. Second, the $S = 0.6$ case shows a large peak at a frequency of $0.45\ U_0/D$. This low-frequency peak, which is not seen in the $S = 0.55$ case, provides strong evidence for the existence of the PVC in the $S = 0.6$ case.

6 Scalar mixing enhancement by Swirl

Next, the unified RANS-LES model will be used for the calculation of the mixing efficiency m_e of scalars depending on the swirl number S, which is very helpful for technical applications (the quantification of swirl effects on the mixing of species in turbulent combustion systems). There are two differences to our previous calculation of the mixing efficiency m_e based on a segregated RANS-LES model [17]: the mixing efficiency calculations presented here (i) include the vortex breakdown regime, and (ii) these calculations are performed with a methodology that was proven to be more accurate than the segregated RANS-LES modeling approach (see the discussions in Sections 5 and 7).

The scalar mixing efficiency m_e is defined as $m_e = 1 - I$, where the intensity of segregation reads

$$I = \frac{\sigma_\phi^2}{\Phi(1 - \Phi)}. \tag{22}$$

Here, σ_ϕ^2 is the variance of the instantaneous passive scalar $\widetilde{\phi}$, which is bounded by zero and one, and Φ is the mean value. The mixing efficiency is bounded by zero and one, $0 \leq m_e \leq 1$: the values $m_e = 0$ and $m_e = 1$ correspond to a completely segregated and a completely mixed scalar, respectively [17]. The simplest way to show that m_e is bounded by zero and one is to prove that $0 \leq I \leq 1$. We consider
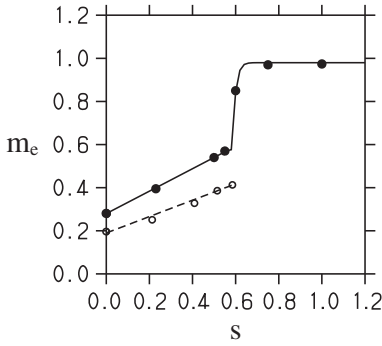
Figure 19: The dependence of the mixing efficiency m_e on the swirl number S for the swirl cases considered. The dots show the m_e values obtained with the unified RANS-LES method. The solid line refers to the model (24). The corresponding results of segregated RANS-LES simulations are given by open circles. The dashed line represents $m_e = 0.185 + 0.378S$.

$$0 \le \left\langle \widetilde{\phi}^2 \right\rangle - \left\langle \widetilde{\phi} \right\rangle^2 = \sigma_\phi^2 \le \left\langle \widetilde{\phi} \right\rangle - \left\langle \widetilde{\phi} \right\rangle^2 = \left\langle \widetilde{\phi} \right\rangle \left(1 - \left\langle \widetilde{\phi} \right\rangle \right). \quad (23)$$

The lower bound is correct because $0 \le \sigma_\phi^2$. The upper bound is correct because $\left\langle \widetilde{\phi}^2 \right\rangle \le \left\langle \widetilde{\phi} \right\rangle$ for a scalar bounded by zero and one. By dividing eq. (23) by $\left\langle \widetilde{\phi} \right\rangle \left(1 - \left\langle \widetilde{\phi} \right\rangle \right)$, which is non-negative, we conclude that $0 \le I \le 1$. Numerically, the calculation of values very close to these limit cases requires care. If $\Phi = 0$ or $\Phi = 1$, we know that the scalar is completely segregated or completely mixed, i.e., $m_e = 0$ or $m_e = 1$, respectively. Therefore, for values $\Phi \le 0.005$ and $\Phi \ge 0.995$ we used $m_e = 0$ or $m_e = 1$, respectively. Further details of the calculation of m_e can be found elsewhere [17].

Figure 19 shows the mixing efficiency m_e obtained by the unified RANS-LES model for the swirl cases considered. In particular, we obtained the values $m_e = (0.280, 0.395, 0.540, 0.570, 0.850, 0.970, 0.974)$ for $S = (0, 0.23, 0.5, 0.55, 0.6, 0.75, 1)$, respectively. The relevance of these mixing efficiency values to the spatial distribution of the passive scalar is illustrated in terms of Figure 20. The unified RANS-LES curve $m_e = f(S)$ shows two trends: a linear dependence for $0 \le S \le 0.58$, which applies to the scalar mixing in absence of vortex breakdown, and an exponential dependence for $0.58 \le S \le 1$, which applies to the vortex breakdown regime. A model for these two trends is given by

$$m_e = \left\{ \begin{array}{ll} 0.28 + 0.52S & if \quad 0 \le S \le 0.58 \\ 0.98 / \left(1 + 0.7 e^{-73(S-0.58)} \right) & if \quad 0.58 \le S \le 1 \end{array} \right\}. \quad (24)$$

These analytical trends represent excellent approximations, the relative error magnitude of the model (24)

is less than 1% and 2% regarding the regimes without and with vortex breakdown, respectively. In particular, the 2% error of the vortex breakdown regime calculation can be seen by the fact that m_e approaches $m_e = 0.98$ for high S values instead of $m_e = 1$. The result of our segregated RANS-LES model in absence of vortex breakdown is also shown in Figure 19. The latter values are given by $m_e = (0.196, 0.251, 0.328, 0.386, 0.413)$ for $S = (0, 0.23, 0.41, 0.5, 0.58)$, respectively. A model for the segregated RANS-LES results, which is also shown in Figure 19, is given by $m_e = 0.185 + 0.378S$. The relative error magnitude of this model is less than 6%.

According to experimental results [28, 65, 66], the turbulent jet growth rate is known to vary linearly with the swirl number in absence of vortex breakdown. Hence, the mixing efficiency of a passive scalar, which is distributed by the turbulent flow structures (the turbulent viscosity is at least 20 times higher than the molecular viscosity for the flows considered), has to show the same linear dependence on the swirl number. Both, the unified and segregated RANS-LES results show the correct linear scaling of the mixing efficiency $m_e = f(S)$ for the regime without vortex breakdown. However, there are differences between the segregated and unified models: the unified RANS-LES model follows better a linear curve and it predicts a significantly higher mixing efficiency than the segregated RANS-LES model. This difference is a consequence of the different modeling concepts applied. The segregated RANS-LES approach combines RANS solutions with artificially generated velocity fluctuations at the jet inlet. This concept can be expected to insufficiently represent the turbulent mixing motions that distribute the scalar (the velocity fluctuations provided at the jet inlet are not solutions of the LES equations). On the other hand, the turbulent mixing motions are more realistically represented by using the unified RANS-LES concept, which applies LES for both the nozzle and jet region. In the presence of vortex breakdown, a rapid transition towards a complete mixing has to be expected because the jet structure of the scalar distribution is broken apart: see Figure 20. This expected behavior can be seen in the unified RANS-LES results (segregated RANS-LES results are unavailable for this regime because of the shortcomings that can be expected).

7 Conclusions

Most RANS methods provide poor predictions of turbulent swirl flows [28–30]. LES including the relevant nozzle
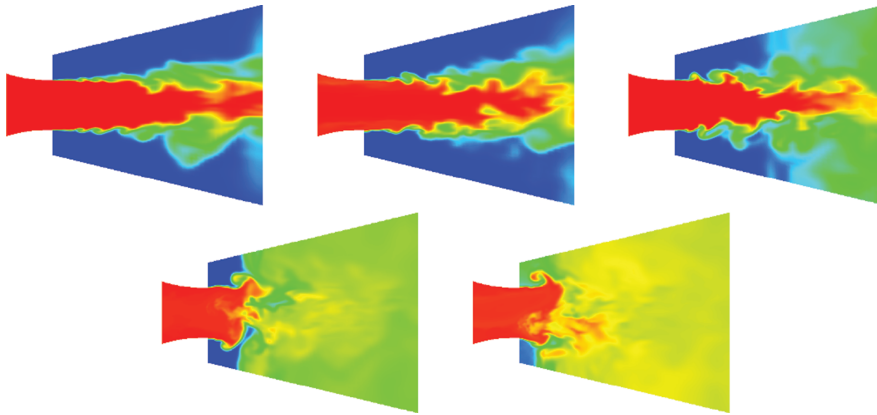
Figure 20: Unified RANS-LES results: Contour plots of instantaneous scalar values in the center-plane $x_3 = 0$ for $S = (0, 0.23, 0.5, 0.75, 1)$ from left to right, respectively. The red color refers to $\widetilde{\phi} = 1$, and the blue color refers to $\widetilde{\phi} = 0$.

flow, which provides the inflow for turbulent jets, are computationally too expensive for the high Reynolds number flows of technical interest. An attractive way to overcome this problem is the use of hybrid RANS-LES methods. A unified RANS-LES method was suggested recently [32], which has been applied to turbulent channel flow simulations [33]. A first objective of this paper was to validate the unified RANS-LES model for turbulent jet flows covering a broad range of swirl numbers by using findings obtained by theory, experiments, and other computational methods. A second objective was to demonstrate the advantages of the unified RANS-LES model in comparison to other hybrid RANS-LES methods. A third objective of this paper was to use the unified RANS-LES results obtained for a better understanding of the mechanism of swirl flows. The results obtained regarding these three objectives will be summarized in the following three paragraphs.

The findings obtained here regarding the validation of the performance of the unified RANS-LES model with respect to turbulent swirl flow simulations can be summarized in the following way. For the nonswirling $S = 0$ case and the $S = 0.23$ case of mild swirl (experimental results are unavailable for other swirl numbers), it was shown that the mean velocities and turbulence intensities predicted by the unified RANS-LES model agree well with experimental results. For higher swirl numbers but in absence of vortex breakdown, the unified RANS-LES method showed that the scalar mixing efficiency increases linearly with the swirl number S, as it has to be expected [28, 65, 66]. Unified RANS-LES simulations showed vortex breakdown for swirl numbers $S \geq 0.6$. The conclusion that $S = 0.6$ represents a critical swirl number required for the onset of vortex breakdown agrees very well with observations made by theory, experiments, and

other computations: see the discussion at the end of Section 5.

There are significant advantages of the unified RANS-LES method in comparison with other hybrid RANS-LES methods. (a) Compared to segregated RANS-LES models, the advantages of the unified approach is a relatively weak dependence on experimental data, which were needed here only to provide nozzle inflow data. On the other hand, the segregated RANS-LES approach requires evidence for the suitability of simulation results at the RANS-LES interface. In addition to the latter fact, the segregated RANS-LES approach may imply inaccurate flow simulations. (b) Compared to DES, the advantage of the unified RANS-LES method presented here is its generality and better performance. In contrast to the unified RANS-LES method, both DES and IDDES suffer from the 'modeled-stress depletion' problem, which results in inappropriate predictions of nonswirling flows (see Section 4) and shortcomings regarding the simulation of other swirling jet flows than considered here [39–41]. In addition, DES results can be significantly affected by model parameter variations [41], whereas the unified RANS-LES model does not involve an adjustable parameter corresponding to C_{DES}.

The unified RANS-LES results presented here contribute to a better understanding of conditions for the onset of vortex breakdown and the mechanism of vortex breakdown. A condition for the onset of vortex breakdown is the requirement to satisfy $R \geq 1$, which requires that the global amount of rotational energy is higher than the kinetic energy in axial direction. This condition was found to be satisfied for $S \geq 0.52$. However, $S \geq 0.52$ does not ensure that vortex breakdown will occur. As argued in Section 5, the occurrence of vortex breakdown requires a slightly higher amount of swirl to stabilize the instantaneous coherent structures involved (the first ring structure

behind the nozzle and recirculation zone). Vortex breakdown was found for $S = 0.6$, which is only slightly higher than the swirl number $S = 0.52$ required for the onset of vortex breakdown. Therefore, knowledge of the swirl number required to satisfy the vortex breakdown criterion $R \geq 1$ provides very valuable information.

References

[1] M. G. Hall, Vortex breakdown, Ann. Rev. Fluid Mech. 4 (1972), 195–218.

[2] D. G. Lilley, Swirl flows in combustion: A review, AIAA J. 15 (8) (1977), 1063–1078.

[3] S. Leibovich, The structure of vortex breakdown, Ann. Rev. Fluid Mech. 10 (1978), 221–246.

[4] A. K. Gupta, D. G. Lilley., N. Syred, Swirl Flows, Abacus Press, Cambridge, MA, 1984.

[5] M. Escudier, Vortex breakdown: Observations and explanations, Progress in Aerospace Sciences 25 (2) (1988), 189–229.

[6] O. Lucca-Negro, T. O'Doherty, Vortex breakdown: A review, Prog. Energy Combust. Sci. 27 (4) (2001), 431–481.

[7] M. R. Ruith, P. Chen, E. Meiburg, T. Maxworthy, Three-dimensional vortex breakdown in swirling jets and wakes: Direct numerical simulation, Journal of Fluid Mechanics 486 (2003), 331–378.

[8] K. Oberleithner, C. O. Paschereit, R. Seele, I. Wygnanski, Formation of turbulent vortex breakdown: Intermittency, criticality, and global instability, AIAA J. 50 (7) (2012), 1437–1452.

[9] K. Oberleithner, M. Sieber, C. N. Nayeri, C. O. Paschereit, C. Petz, H.-C. Hege, B. R. Noack, I. Wygnanski, Three-dimensional coherent structures in a swirling jet undergoing vortex breakdown: Stability analysis and empirical mode construction, Int. J. Fluid Mech. 679 (2011), 383–414.

[10] W. Kollmann, Accurate numerical simulations of vortex flows. i: Vortex breakdown, Comput. Fluids 41 (1) (2011), 103–109.

[11] W. Kollmann, Accurate numerical simulations of vortex flows ii: Interaction of swirling vortex rings, Comput. Fluids 41 (1) (2011), 110–118.

[12] M.-Z. P. Ismadi, P. Meunier, A. Fouras, K. Hourigan, Experimental control of vortex breakdown by density effects, Phys. Fluids 23 (3) (2011), 034104/1–9.

[13] M. Jones, A. Hashimoto, Y. Nakamura, Criteria for vortex breakdown above high-sweep delta wings, AIAA J. 47 (10) (2009), 2306–2320.

[14] A. Mitchell, J. Délery, Research into vortex breakdown control, Prog. Aerosp. Sci. 37 (4) (2001), 385–418.

[15] R. T. Gilchrist, J. W. Naughton, Experimental study of incompressible jets with different initial swirl distributions: Mean results, AIAA J. 43 (4) (2005), 741–741.

[16] R. T. Gilchrist, J. W. Naughton, The design of a swirling jet facility, in: 40th AIAA Aerospace Sciences Meeting and Exhibit, AIAA Paper 02-0442, Reno, NV, 2002.

[17] C. P. Zemtsop, M. K. Stöllinger, S. Heinz, D. Stanescu, Large eddy simulation of swirling turbulent jet flows in absence of vortex breakdown, AIAA J. 47 (12) (2009), 3011–3021.

[18] W. Kollmann, A. S. H. Ooi, M. S. Chong, J. Soria, Direct numerical simulations of vortex breakdown in swirling jets, J. Turbul. 2 (2001), 1–17.

[19] S. McIlwain, A. Pollard, Large eddy simulation of the effects of mild swirl on the near field of a round free jet, Phys. Fluids 14 (2) (2002), 653–661.

[20] A. Kempf, W. Malalasekera, K. K. J. Ranga-Dinesh, O. Stein, Large eddy simulations of swirling non-premixed flames with flamelet models: A comparison of numerical methods, Flow, Turbul. Combust. 81 (4) (2008), 523–561.

[21] Y. Yang, S. K. Kær, Comparison of Reynolds averaged Navier-Stokes based simulation and large-eddy simulation for one isothermal swirling flow, J. Therm. Sci. 21 (2) (2012), 154–161.

[22] Y. Maciel, L. Facciolo, C. Duwig, L. Fuchs, P. Alfredsson, Near-Field Dynamics of a Turbulent Round Jet with Moderate Swirl, Int. J. Heat Fluid Flows 29 (3) (2008), 675–686.

[23] S. Müller, L. Kleiser, Large-Eddy Simulation of Vortex Breakdown in Compressible Swirling Jet Flow, Comput. Fluids 37 (7) (2008), 844–856.

[24] M. García-Villalba, J. Fröhlich, W. Rodi, Identification and analysis of coherent structures in the near field of a turbulent unconfined annular swirling jet using large eddy simulation, Phys. Fluids 18 (5) (2006), 055103/1–17.

[25] M. García-Villalba, J. Fröhlich, W. Rodi, Numerical simulations of isothermal flow in a swirl burner, J. Eng. Gas Turbines Power 129 (2) (2007), 377–386.

[26] J. Fröhlich, M. García-Villalba, W. Rodi, Scalar mixing and large-scale coherent structures in a turbulent swirling jet, Flow Turbul. Combust. 80 (1) (2008), 4759.

[27] J. D. Chenoweth, B. York, A. Hosangadi, Turbulence model upgrades for swirling flows, in: 5th Joint ASME/JSME Fluids Engineering Conference, American Society of Mechanical Engineers (ASME), FEDSM2007-37163/1-8, San Diego, CA, 2007.

[28] J. D. Chenoweth, C. Kannepalli, S. Arunajatesan, A. Hosangadi, Modeling swirling jet flows using a hybrid rans/les methodology, in: 44th AIAA/ASME/SAE/ASEE Joint Propulsion

Conference, American Institute of Aeronautics and Astronautics (AIAA), AIAA Paper 08-4746/1-14, Hartford, CT, 2008.

[29] S. Jakirlić, K. Hanjalić, C. Tropea, Modeling rotating and swirling turbulent flows: A perpetual challenge, AIAA J. 40 (10) (2002), 1984–1996.

[30] B. A. Younis, T. B. Gatski, C. G. Speziale, Assessment of the SSG pressure-strain model in free turbulent jets with and without swirl, J. Fluids Eng. 118 (1996), 800–809.

[31] A. Smirnov, S. Shi, I. Celik, Random flow generation technique for large eddy simulations and particle-dynamics modeling, J. Fluids Eng. 123 (2) (2001), 359–371.

[32] S. Heinz, Unified turbulence models for LES and RANS, FDF and PDF simulations, Theor. Comput. Fluid Dyn. 21 (2) (2007), 99–118.

[33] H. Gopalan, S. Heinz, M. Stöllinger, A unified RANS-LES model: Computational development, accuracy and cost, J. Comput. Phys. 249 (2013), 249–279.

[34] P. Spalart, W.-H. Jou, M. Strelets, S. Allmaras, Comments on the feasibility of LES for wings, and on a hybrid RANS/LES approach, in: In C. Liu and Z. Liu, (Eds.), Advances in DNS/LES, 1st AFOSR International Conference on DNS/LES, pp. 137–147, Columbus, OH, Greyden Press, 1997.

[35] P. R. Spalart, Detached-eddy simulation, Ann. Rev. Fluid Mech. 41 (2009), 181–202.

[36] S. Deck, Zonal-detached-eddy simulation of the flow around a high-lift configuration, AIAA J. 43 (11) (2005), 2372–2384.

[37] N. Chauvet, S. Deck, L. Jacquin, Zonal detached eddy simulation of a controlled propulsive jet, AIAA J. 45 (10) (2007), 2458–2373.

[38] D. C. Wilcox, Turbulence Modeling for CFD, 2nd Edition, DCW Industries, Canada, 1998.

[39] C. De Langhe, J. Bigda, K. Lodefier, E. Dick, One-equation RG hybrid RANS/LES computation of a turbulent impinging jet, J. Turbul. 9 (16) (2008), 1–19.

[40] P. G. Tucker, Novel miles computations for jet flows and noise, Int. J. Heat Fluid Flow 25 (4) (2004), 625–635.

[41] C. De Langhe, B. Merci, E. Dick, Application of a RG hybrid RANS/LES model to swirling confined turbulent jets, J. Turbul. 7 (56) (2006), 1–19.

[42] M. L. Shur, P. R. Spalart, M. K. Strelets, A. K. Travin, A hybrid RANS-LES approach with delayed-des and wall-modelled LES capabilities, Int. J. Heat Fluid Flow 29 (6) (2008), 1638–1649.

[43] S. Heinz, Statistical Mechanics of Turbulent Flows, Springer-Verlag, Berlin, 2003.

[44] S. Heinz, On Fokker-Planck Equations for Turbulent Reacting Flows. Part 1. Probability Density Function for Reynolds-Averaged Navier–Stokes Equations, Flow, Turbul. Combust. 70 (1-4) (2003), 115–152.

[45] S. Heinz, On Fokker-Planck Equations for Turbulent Reacting Flows. Part 2. Filter Density Function for Large Eddy Simulation, Flow, Turbul. Combust. 70 (1-4) (2003), 153–181.

[46] S. Heinz, Mathematical Modeling, 1st Edition, Springer-Verlag, Heidelberg, Dordrecht, London, New York, 2011.

[47] J. Bredberg, S. Peng, L. Davidson, An Improved k-ω Turbulence Model Applied to Recirculating Flows, Int. J. Heat Fluid Flow 23 (6) (2002), 731–743.

[48] Openfoam, the open source CFD tool box, user guide, version 1.6, see www.openfoam.org, Tech. rep. (2009).

[49] S. B. Pope, Turbulent Flows, Cambridge University Press, Cambridge, UK, 2000.

[50] M. Strelets, Detached eddy simulation of massively separated flows, in: 39th AIAA Aerospace Sciences Meeting and Exhibit, AIAA Paper 01-0879, Reno, NV, 2001.

[51] A. Travin, M. Shur, M. Strelets, P. R. Spalart, Physical and numerical upgrades in the detached-eddy simulation of complex turbulent flows, in: R. Friedrich and W. Rodi (Eds.) Fluid Dynamics and Its Applications. Advances in LES of Complex Flows, Proceedings of EUROMECH Colloquium, Vol. 412, pp. 239–254, Kluwer Academic, Dordrecht, 2002.

[52] F. R. Menter, Zonal two-equation $k - \omega$ turbulence models for aerodynamic flows, in: 24th Fluid Dynamics Conference, AIAA Paper 93-2906, Orlando, FL, 1993.

[53] F. R. Menter, M. Kuntz, R. Langtry, Ten years of industrial experience with the sst turbulence model, in: In: K. Hanjalić and Y. Nagano and M. Tummers (Eds.), Turbulence, Heat and Mass Transfer 4, Proceedings of EUROMECH Colloquium, pp. 625–632, Begell House, 2003.

[54] C. Hasse, V. Sohm, M. Wetzel, B. Durst, Hybrid URANS/LES Turbulence Simulation of Vortex Shedding Behind a Triangular Flameholder, Flow, Turbul. Combust. 83 (1) (2009), 1–20.

[55] F. R. Menter, Two-equation eddy-viscosity turbulence models for engineering applications, AIAA J. 32 (8) (1994), 1598–1605.

[56] U. Piomelli, Large-eddy simulations: where we stand, in: C. Liu, Z. Liu, L. Sakell (Eds.), Advances in DNS/LES, pp. 93–104, Greyden Press, Columbus, Ohio, 1997.

[57] R. Issa, Solution of the Implicitly Discretized Fluid Flow Equations by Operator-Splitting, J. Comput. Phys. 62 (1) (1986), 40–65.

[58] S. Komori, H. Ueda, Turbulent flow structure in the near field of a swirling round free jet, Phys. Fluids 28 (7) (1985), 2075–2082.

[59] P. Billant, J. Chomaz, P. Huerre, Experimental study of vortex breakdown in swirling jets, J. Fluid Mech. 376 (1998), 183–219.

[60] D. G. Syred, J. Beer, Combustion in swirling flows: A review, Combust. Flame 23 (2) (1974), 143–201.

[61] S. Farokhi, R. Taghavi, E. Rice, Effect of initial swirl distribution on the evolution of a turbulent jet, AIAA J. 27 (6) (1989), 700–706.

[62] R. F. Huang, F. C. Tsai, Flow field characteristics of swirling double concentric jets, Exp. Therm Fluid Sci. 25 (3-4) (2001), 151–161.

[63] N. Syred, A review of oscillation mechanisms and the role of the precessing vortex core (pvc) in swirl combustion systems, Prog. Energy Combust. Sci. 32 (2) (2006), 93–161.

[64] F. Martinelli, A. Olivani, A. Coghe, Experimental analysis of the precessing vortex core in a free swirling jet, Exp. Fluids 42 (6) (2007), 827–839.

[65] N. A. Chigier, A. Chervinsky, Experimental investigation of swirling vortex motion in jets, J. Appl. Mech. 34 (2) (1967), 443–451.

[66] A. Shiri, W. K. George, J. W. Naughton, Experimental study of the far field of incompressible swirling jets, AIAA J. 46 (8) (2008), 2002–2009.